Journal of Power Sources 196 (2011) 8323–8330

Contents lists available at ScienceDirect

Journal of Power Sources

journal homepage: www.elsevier.com/locate/jpowsour

Carbon-supported PtAu alloy nanoparticle catalysts for enhanced electrocatalytic oxidation of formic acid

Guoqin Chen[a], Yunhua Li[a], Dong Wang[a], Li Zheng[a], Guirong You[a], Chuan-Jian Zhong[b], Lefu Yang[a], Fan Cai[a], Junxiu Cai[a], Bing H. Chen[a,*]

[a] College of Chemistry and Chemical Engineering, National Engineering Laboratory for Green Chemical Productions of Alcohols–Ethers–Esters, Xiamen University, Xiamen 361005, China
[b] Department of Chemistry, State University of New York at Binghamton, Binghamton, NY 13902, USA

ARTICLE INFO

Article history:
Received 8 May 2011
Received in revised form 12 June 2011
Accepted 14 June 2011
Available online 21 June 2011

Keywords:
Bimetallic catalysts
Electrocatalysts
Electrooxidation of formic acid
Platinum–gold alloy
Fuel cells

ABSTRACT

The understanding of the electrocatalytic activity of bimetallic nanoparticle catalysts requires the ability to precisely control the composition and phase properties. In this report, we describe a new strategy in the preparation of a series of carbon supported platinum–gold bimetallic nanoparticles with various bimetallic compositions which were loaded onto a carbon black support and subjected subsequently by thermal treatment ($Pt_{100-m}Au_m$/C). The $Pt_{100-m}Au_m$/C catalysts are characterized by X-ray diffraction (XRD), transmission electron spectroscopy (TEM), and induced coupled plasma-atomic emission spectroscopy (ICP-AES). The XRD pattern for the bimetallic nanoparticles shows single-phase alloy character. This ability enabled us to establish the correlation between the bimetallic composition and the electrocatalytic activity for formic acid (FA) electrooxidation. The electrocatalytic activities of the catalysts toward FA oxidation reaction are shown to strongly depend on the bimetallic PtAu composition. Within a wide range of bimetallic composition, the $Pt_{50}Au_{50}$/C catalyst shows the highest electrocatalytic activity for the FA oxidation, with a mass activity eight times higher than that of Pt/C. The high performance of the PtAu/C catalyst can be ascribed to the increased selectivity toward the FA dehydrogenation at the decreased availability of adjacent Pt atoms.

1. Introduction

Direct formic acid fuel cells (DFAFCs) are considered as a promising fuel–cell system for portable electronic applications owing to its high energy density, fast oxidation kinetics, convenience of liquid formic acid (FA), non-toxic nature of FA, and simplicity of power system integration [1]. FA exhibits a smaller crossover flux through Nafion than methanol, allowing the use of highly concentrated fuel solutions and thinner membranes [2]. In addition, DFAFCs technology has shown superior electrocatalytic oxidation activity in comparison with direct methanol fuel cells (DMFCs) and the performances approaching those of H_2-PEM fuel cells in some cases [3]. However, the commercialization of DFAFCs is impeded by poor performance of catalysts for FA electrooxidation [1].

Platinum- and palladium-based materials are the most commonly used electrocatalysts for FA oxidation [4–6]. The Pd-based catalysts exhibit a very high initial activity due to being free of CO poisoning [7]. However, significant performance losses occur due to the vulnerability of the catalysts toward uncharacterized intermediate species [8] and the potential for the dissolution of Pd in acidic solutions [9]. There have been also studies of FA electrooxidation at Pt electrode. It has been widely accepted that the mechanism of FA oxidation at Pt electrode involves the so-called dual-pathway mechanism: a direct pathway to CO_2 via a reactive intermediate (dehydrogenation pathway) and an indirect pathway via adsorbed $CO(CO_{ad})$ intermediate which is oxidized to CO_2 at high potentials (dehydrate pathway) [10].

Although pure Pt catalyst is easily poisoned by adsorbed $CO(CO_{ad})$, a reaction intermediate [10], one tactic to improve catalytic activity is to form binary platinum-based catalysts. Several bimetallic Pt–M (M = Pd, Bi, Pb, Sb, Ru, Fe and Au) catalysts have been investigated extensively [11–17]. For instance, the promotion of Bi on the PtBi catalysts was ascribed to a combination of the ensemble and electronic effects [12], though bifunctional activity of hydroxylated Bi species was also considered [18]. The activity of Ru was discussed in terms of the bifunctional mechanism [15]. PtFe and PtAu alloys also show markedly improved activity toward FA oxidation via the ensemble effect [16,17]. Pt-based alloy catalysts typically display enhanced catalytic activity toward FA oxidation that has been attributed to the so-called bifunctional, ensemble and/or electronic effects.

* Corresponding author. Tel.: +86 592 2185253; fax: +86 592 2184822.
E-mail address: chenbh@xmu.edu.cn (B.H. Chen).

0378-7753/$ – see front matter © 2011 Elsevier B.V. All rights reserved.
doi:10.1016/j.jpowsour.2011.06.048

Among all these alloys tested, the Pt–Au catalyst has been shown to be one of the most promising catalysts in terms of the catalytic activity and stability [19]. In previous studies of Pt–Au bimetallic catalyst systems, it have been found that the electrocatalytic activity depends strongly on the surface structure because of the variation of the density of active sites [20–23]. Examples include Pt sub-monolayers on Au nanorod [20], Pt-around-Au nanoparticles [21], Pt-on-Au nanoparticles [22] and nanoporous Au–Pt–Au sandwich-type nanostructure [23], which have been explored to address the catalyst activity, durability, and cost. For Pt–Au binary alloy catalysts, the choice of the preparative method has played an important role in controlling the size, composition and phase properties of the catalyst. Zhao and co-workers prepared $Pt_{50}Au_{50}$ alloy nanoparticles by co-reduction method in N,N-dimethylformamide (DMF), which showed about 35% higher power density than the cell with Pt/C catalyst for formic acid oxidation reaction [19]. Similarly, Lin and co-workers showed that $Pt_{50}Au_{50}$/C catalyst prepared by co-reduction method in the presence of sodium citrate exhibited higher activity toward formic acid oxidation than Pt/C electrocatalyst due to the optimal tolerance to CO poisoning [17]. Huang et al. investigated the effects of Au on the electrooxidation activity of formic acid using electrospun carbon nanofiber-supported PtAu bimetallic nanoparticles (average diameter = 118 nm) prepared by electrodeposition method. The catalyst exhibited improved electrocatalytic activities than Pt/CNF [24]. Sung and co-workers investigated PtAu alloy as an anodic catalyst in the direct liquid (methanol and formic acid) fuel cell, showing a higher activity than that of commercial PtRu [25]. They also studied the influence of Au contents on the electrooxidation activity of formic acid with unsupported PtAu catalysts prepared by impregnation reduction method which were generally < 10 nm in diameter but with a significant degree of aggregation. The catalyst showed a lower onset potential and higher current density than Pt [26]. While the mechanistic details for the enhanced electrocatalytic activity of PtAu nanoparticle catalysts have not been established, these previous studies suggest that in addition to surface structure the bimetallic composition also acts as a very important parameter to manipulate the catalytic activity. It is important to point out that the controllability over the size and composition of the catalyst particles in these previous studies has been rather limited because of the choice of the preparative method. This limitation makes the comparison of catalytic activities difficult and hampers the establishment of the composition–activity relationships, which are critical for rational design of highly efficient and active catalysts. Therefore, a systematic study of the influence of the bimetallic composition on the electrocatalytic activity is needed, which calls for improved methods in the synthesis of the alloy nanoparticles with well-controlled sizes and compositions.

The control over size, composition, and phase properties of the carbon-supported PtAu nanoparticles have been shown to depend on a combination of preparation parameters (e.g., temperature, support, etc.) [27,28]. $Pt_{100-m}Au_m$/C catalysts were found to exhibit excellent electrocatalytic activities for methanol electrooxidation and oxygen reduction reaction [29,30]. In this work, we have refined the preparation parameters for the control of the size and composition, which is aimed at establishing the correlation between the catalytic activity and the bimetallic composition of the carbon-supported PtAu alloy nanoparticles toward FA electrooxidation. A series of monodispersed PtAu alloy nanoparticles with different atomic ratios were prepared by a modified two-phase method and subsequent assembly on carbon black support and thermal treatment ($Pt_{100-m}Au_m$/C). The ability to control the size, composition, phase properties of the $Pt_{100-m}Au_m$/C catalysts enabled us to establish the correlation between the bimetallic composition and the electrocatalytic activity for FA electrooxidation. New insights into the promotion of Au in the bimetallic catalysts for the active and selective electrocatalytic oxidation of FA are also discussed.

2. Experimental

2.1. Chemicals

Hydrogen tetrachloroaurate ($HAuCl_4$, 99%), tetraoctylammonium bromide (TOABr, 99%), hydrogen hexachloroplatinate (IV) ($H_2PtCl_6{\cdot}XH_2O$, 99.995%), $NaBH_4$, oleylamine ($CH_3(CH_2)_7CH{=}CH(CH_2)_8{-}NH_2$, 70%), and other solvents such as ethanol, acetone, toluene and hexane were purchased from Sinopharm Chemical Reagent Co. Ltd. (Shanghai, China) and used as received. Carbon black (XC-72R) was obtained from Cabot. Nafion solution (5 wt%) was purchased from Aldrich and used as received. Water was purified with a Millipore Milli Q system.

2.2. Synthesis of PtAu nanoparticles

Oleylamine-capped platinum–gold (PtAu) nanoparticles were prepared using a modified two-phase protocol [31,32]. The preparation of $Pt_{50}Au_{50}$ nanoparticles is described here as an example for the preparation procedure and details. Under vigorous stirring, an aqueous solution of $H_2PtCl_6{\cdot}XH_2O$ (0.126 g, 0.243 mmol) and $HAuCl_4$ (0.1 g, 0.243 mmol) were combined with a toluene solution of TOABr (0.8 g, 1.456 mmol), resulting in a deep-red mixture. After the mixture was stirred for 10 min and the water phase was separated from the toluene phase, 1 mL oleylamine was added to the toluene phase to form a bright orange–yellow mixture. Subsequently, a freshly made aqueous solution (5 mL) of $NaBH_4$ (0.258 g, 6.8 mmol) was rapidly added as a reduction agent, quickly the mixture turned into a dark brown as the PtAu nanocrystals formed. After further stirring for 4 h, the aqueous phase was discarded, and the volume of the toluene phase was reduced to around 4 mL by using a rotary evaporator. Immediately, ethanol (80 mL) was added to the toluene for dispersion, and the mixture was precipitated out via centrifugation at 3000 rpm for 20 min. The nanoparticles were then collected on a glass filtration frit, and washed with at least 100 mL ethanol and 100 mL acetone. The as-synthesized oleylamine-capped PtAu nanoparticles were dispersed in 10 mL hexane for further use.

2.3. Assembly of PtAu nanoparticles on carbon and subsequent thermal treatment

For the assembly of the nanoparticles on carbon support, a suspension of 100 mg carbon black (Vulcan XC-72) in 100 mL hexane was sonicated at room temperature for 1 h, followed by addition of 40 mg PtAu nanoparticles. The suspension was sonicated for 30 min, followed by stirring overnight. The product (PtAu supported on carbon) was precipitated out via centrifugation at 3000 rpm for 10 min, and then collected and dried under N_2 atmosphere. Loading PtAu nanoparticles on carbon support was controlled by the weight ratio of the nanoparticles versus carbon black while the actual loading of metals was determined by ICP-AES measurements.

The above resultant powder was thermally treated in a tube-furnace under controlled temperatures and atmospheres. A typical protocol includes shell removal by heating at 300 °C under 20% O_2/N_2 for 30 min, and then treated at 400 °C under 10% H_2/N_2 for 1 h for calcination.

2.4. Characterization

The HR-TEM images of the samples were obtained on a Technai F30 microscope at an accelerating voltage of 300 kV. Specimens

were prepared by ultrasonically suspending the samples in hexane solution, which were then applied to a copper grid and dried in air.

Powder X-ray diffraction (XRD) spectra were measured on a Panalytical X'Pert PRO X-ray diffractometer using Cu Kα radiation (k = 1.54056 Å), operated at 40 kV and 30 mA. Diffraction patterns were collected from 30 to 90° at a scanning rate of 5° per minute, and with a step size of 0.02°. The mean particle size was calculated from the (2 2 0) diffraction plane using the Scherrer equation.

The loading and composition of the as-synthesized PtAu/C catalysts were determined by inductively coupled plasma atomic emission spectroscopy (ICP-AES). In this analysis, the PtAu/C samples were digested in concentrated aqua regia at ca. 60 °C overnight, and then diluted with water to concentrations between 1 and 50 ppm as a working solution for analysis. Measurements were made on emission peaks at 267.588 and 265.945 nm, for Au and Pt, respectively. The average values were compared to the interpolation of the ICP-AES results for each working solution on a calibration plot made from standard samples in order to precisely calculate the loading and composition of Au and Pt for each working solution.

2.5. Electrochemical measurements

Electrochemical measurements were performed using a conventional three-electrode electrochemical cell with a Pt wire and a saturated calomel electrode (SCE) serving as the counter and the reference electrodes, respectively. A glassy carbon (GC) disk coated with a layer of catalysts was used as the working electrode. The GC electrode was initially polished with 1, 0.3, and 0.05 μm Al_2O_3 slurries. It was cleaned by sonication in Millipore water for 3 min after each polishing step and then dried after washing with water. The ink of carbon-supported catalysts was prepared by ultrasonically dispersing 10 mg of catalyst powders to 4 mL ultrapure water, 1 mL isopropanol and 30 μL of 0.25% Nafion solution, followed by sonication at room temperature for 10 min. Exactly 10 μL of this catalyst ink was pipetted onto the surface of the glassy carbon disk electrode (geometric area of 0.196 cm^2) and dried by IR lamp.

All electrochemical experiments were carried out at room temperature (25 ± 1 °C), and the electrolyte solutions were de-aerated with high purity nitrogen before the measurements. All potentials are given with respect to SCE. For electrochemical surface area (ECSA) measurements, the electrodes were scanned in the range of −0.2 to 1.2 V in a 0.5 M H_2SO_4 solution for 20 cycles at a scan rate of 100 mV s^{-1} until a stable curve was obtained. For electrocatalytic oxidation of FA, the electrolytes were cycled between −0.2 and 1 V in a 0.5 M H_2SO_4 and 1 M FA solution at a scan rate of 50 mV s^{-1}. The amperometric current density–time (i–t) curves were measured at a controlled potential of 0.1 V for 2000s. For CO stripping voltammetry measurements, CO gas (99.99%) was bubbled through the electrolyte for 15 min while keeping the electrode potential at −0.1 V. After purging the electrolyte by N_2 for 20 min to eliminate the dissolved CO, the adsorbed CO was oxidized in an anodic scan at 20 mV s^{-1}.

3. Results and discussion

3.1. Size and composition of PtAu nanoparticles and PtAu/C catalysts

Fig. 1 shows a typical set of TEM micrographs and size distribution histograms of the as-prepared $Pt_{50}Au_{50}$ nanoparticles. It is evident that the vast majority of the particles exhibit a core diameter close to 2.6 nm with no apparent aggregation, and the core size distributions are all very narrow (±0.5 nm). The composition of the $Pt_{100-m}Au_m$ nanoparticles was tuned by simply varying the stoichiometic ratio of the Pt and Au precursors in the synthesis, where the value of m ranged from 30 to 70.

The as-prepared nanoparticles were loaded onto carbon supports, and subsequently underwent thermal treatment. The removal of the shell components after the thermal treatment was examined by XPS. The peaks corresponding to N species (N_{1S}, 399.3 eV) were not detected in the XPS spectrum (not shown), demonstrating an effective removal of the capping molecules. Fig. 2 shows a representative set of TEM micrographs for three different samples of PtAu/C catalysts ($Pt_{60}Au_{40}$/C, $Pt_{50}Au_{50}$/C, and $Pt_{30}Au_{70}$/C). Despite the high annealing temperatures, the dispersion of the PtAu nanoparticles supported on carbon remains relatively high. Most of the post-treatment nanoparticles were in the size range of 4.5–5.5 nm, with only a small fraction of particles larger than 6 nm. Because of the high monodispersity of the particle size, we were able to establish the correlation between the bimetallic composition of the PtAu/C catalysts and the electrocatalytic activity for FA electrooxidation.

3.2. Phase properties of the PtAu/C catalysts

To determine the morphological and structural characteristics of carbon-supported bimetallic nanoparticles with varying Pt to Au atomic ratios, the nanoparticles were characterized by XRD. A typical set of XRD data is shown in Fig. 3A. The diffraction patterns for the carbon-supported nanoparticles indicate a series of broad Bragg peaks, characteristic of materials of limited structural coherence. Nevertheless, the peaks are defined well enough to allow a definitive phase identification and structural characterization.

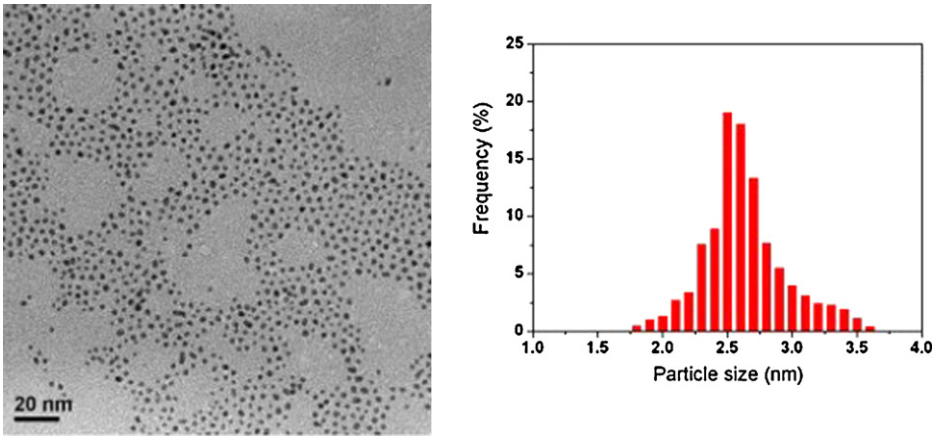

Fig. 1. TEM micrographs and size distributions of oleylamine-capped $Pt_{50}Au_{50}$ nanoparticles (2.6 ± 0.5 nm).

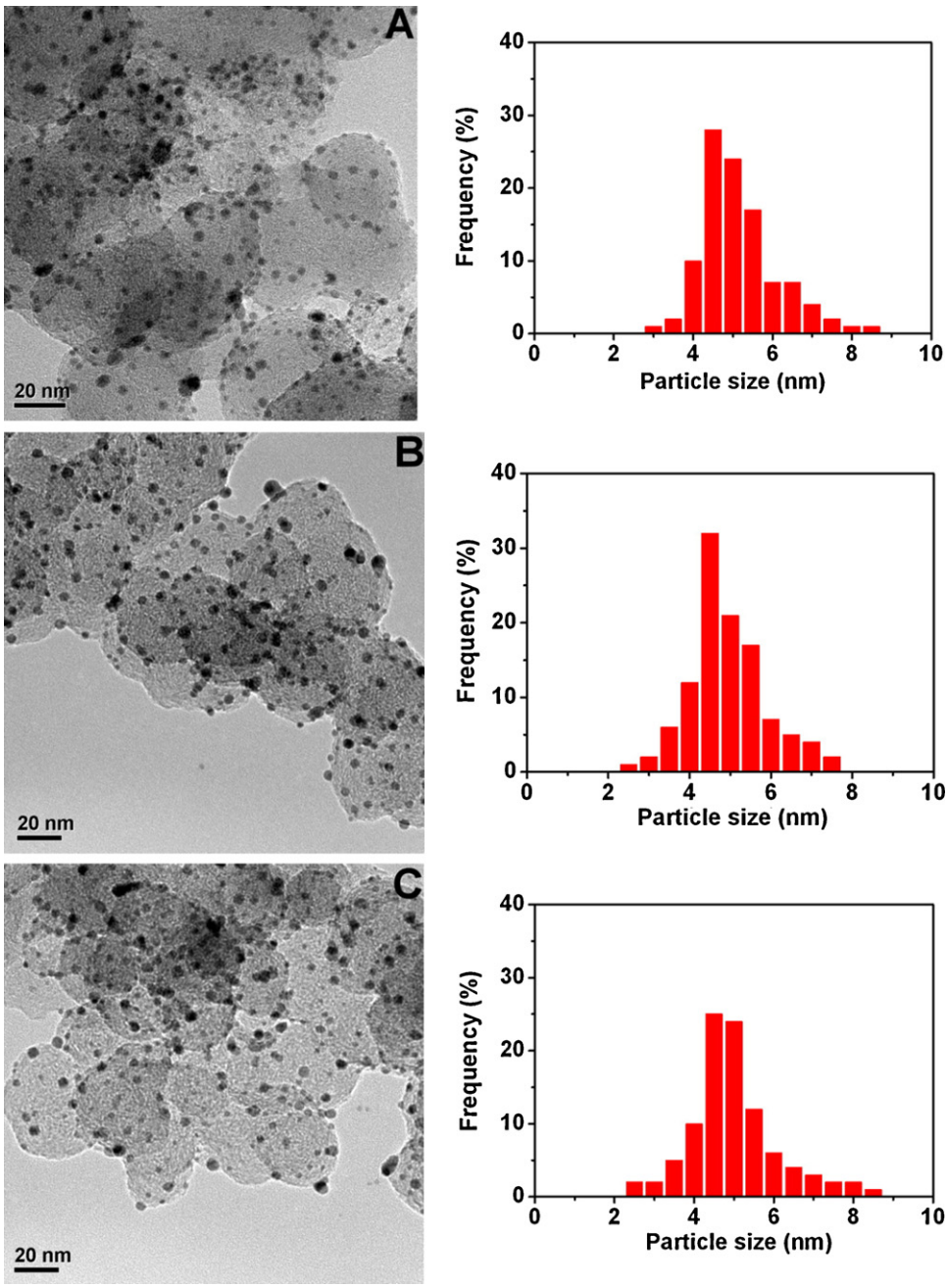

Fig. 2. TEM micrographs and size distributions for $Pt_{60}Au_{40}$/C (A), $Pt_{50}Au_{50}$/C (B) and $Pt_{30}Au_{70}$/C (C) after thermal treatment at 400 °C, and the average diameter are 4.8 ± 1.3 nm, 4.5 ± 1.5 nm and 5.1 ± 1.1 nm, respectively.

The diffraction patterns of Au/C and Pt/C could be unambiguously indexed into an fcc-type cubic lattice occurring with bulk gold and platinum. The peaks around 38.24°, 44.79°, 65.58°, and 78.13° are assigned to Au-(1 1 1), -(2 0 0), -(2 2 0), and -(3 1 1), respectively, and the peaks around 39.82°, 46.55°, 67.89°, and 82.38° are assigned to Pt-(1 1 1), -(2 0 0), -(2 2 0), and -(3 1 1) respectively. We obtained the corresponding lattice parameters by carefully determining the positions of all Bragg peaks in the diffraction patterns. For gold on carbon we obtained a lattice parameter of $a = 4.067$ Å, which is slightly smaller than the literature value of 4.078 Å for bulk gold. For platinum on carbon we obtained a lattice parameter of $a = 3.921$ Å. It is shorter than the lattice parameter of bulk platinum: $a = 3.97$ Å. These observations are consistent with the lattice shrinking for small-sized particles [26].

The X-ray diffraction patterns of $Pt_{100-m}Au_m$ nanoparticles exhibit four major peaks, which can be assigned to PtAu-(1 1 1), -(2 0 0), -(2 2 0), -(3 1 1) planes of the face-centered cubic lattice for PtAu nanoparticles. These peaks fall well between the peaks of Au and Pt nanoparticles and perfectly fit with a single analytical function, suggesting that the PtAu nanoparticles are indeed single-phase PtAu alloy. Moreover, those patterns show a smooth transition from a Pt/C-like pattern to an Au/C-like pattern with the increase of Au content. This observation indicates that $Pt_{100-m}Au_m$/C catalysts bear the characteristics of an alloy type compound involving Au and Pt. To verify the assessment quantitatively, we carefully calculated the lattice parameters of the corresponding alloys with different composition. The lattice parameters are presented in Fig. 3B. They were found to scale lin-

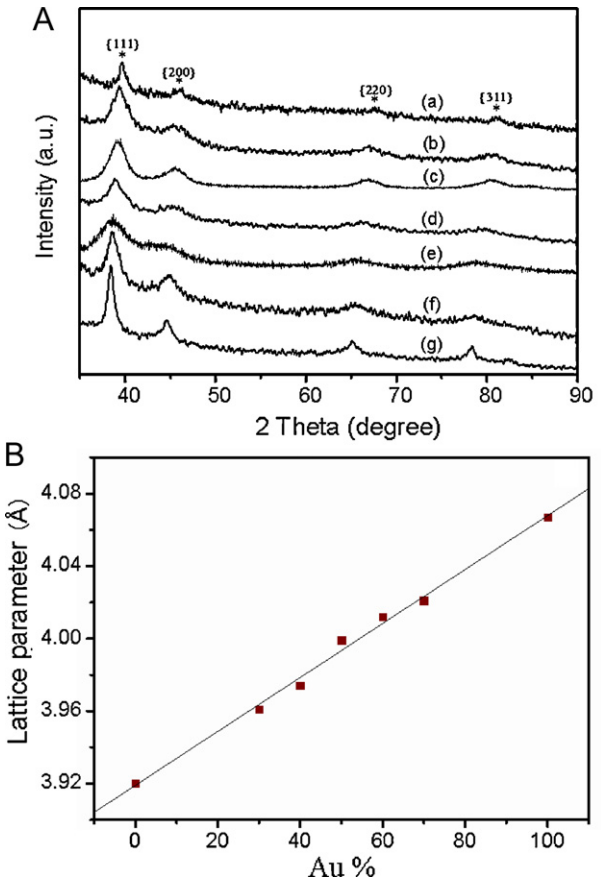

Fig. 3. (A) XRD patterns for Pt/C (a), $Pt_{70}Au_{30}$/C (b), $Pt_{60}Au_{40}$/C (c), $Pt_{50}Au_{50}$/C (d), $Pt_{40}Au_{60}$/C (e), $Pt_{30}Au_{70}$/C (f), Au/C (g) catalysts. (B) The experimental lattice parameters of PtAu nanoparticles (symbols) on the relative composition of Au %. The black line is a linear fit to the experimental data.

early with the relative Pt/Au content. In other words, they follow a Vegard's law [27], indicating that the nanoparticles are an alloy rather than a mixture of monometallic or core–shell nanoparticles. For the mixture of monometallic or core–shell nanoparticles, the linear correlation between the lattice parameter and the composition always breaks in a content range from 10 to 80% Au, within this miscibility gap, the lattice parameters corresponding to bulk crystalline PtAu samples are independent on composition. Whereas the lattice parameters of the PtAu alloy samples well fit with the linear correlation. This finding shows that the correlation between the phase property and the bimetallic composition for nanoscale materials is different from their bulk counterparts, which is consistent with the findings in previous reports [27,28]. Recently, the evolution of the relative surface composition of Pt and Au in the AuPt nanoparticles as a function of temperature was substantiated by XPS. The data confirmed that the AuPt nanoparticles are alloys when they were treated at 400 °C [28]. This information was considered for assessing the evolution of the relative surface composition of Pt and Au in the AuPt nanoparticles as a function of temperature and for the correlation between the phase structures and the activity and stability for formic acid electrooxidation.

The mean diameters of the nanoparticles were evaluated from the XRD patterns for $Pt_{100-m}Au_m$/C catalysts according to the Scherrer formula (Eq. (1)):

$$D = \frac{K\lambda}{\beta \cos\theta} \quad (1)$$

where D is the average particle size, $K = 0.89$, $\lambda = 0.15406$, θ is the angle of the (2 2 0) peak maximum, and β is the width in radians of the diffraction peak at half height. The mean diameters of $Pt_{100-m}Au_m$ alloy nanoparticles estimated from the half-width of the (2 2 0) diffraction peak are summarized in Table 1. The results reveal that the mean diameters of $Pt_{100-m}Au_m$ alloy nanoparticles are around 5 nm, which is in good agreement with the TEM results.

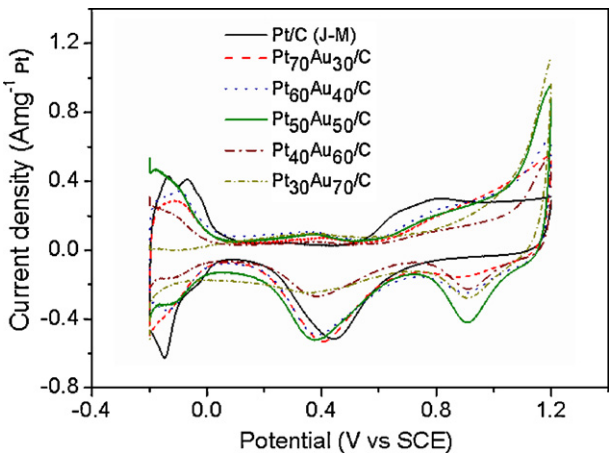

Fig. 4. Cyclic voltammograms for $Pt_{100-m}Au_m$/C catalysts in N_2-saturated 0.5 M H_2SO_4 with a scan rate of 100 mV s^{-1}.

3.3. Electrochemical properties of the $Pt_{100-m}Au_m$/C catalysts

Fig. 4 shows cyclic voltammetry (CV) for the Pt/C (*J–M*) and PtAu/C electrocatalysts in deaerated 0.5 M H_2SO_4 aqueous electrolytes. Typical features characteristic of hydrogen underpotential formation/stripping (H_{UPD}) [33] are clearly observed in the CV curves for all catalysts. The electrochemical surface area (ECSA) for each electrode was calculated from the corresponding charge of H_{UPD} (also known as "hydrogen adsorption") peak divided by the formation charge of a H_{UPD} monolayer deposited on polycrystalline platinum surface (210 μC cm^{-2}) [16]. The ECSA values derived from the integrated areas under the desorption peaks are shown in Table 1. The smaller value of ECSA for PtAu catalysts is attributed to the larger particle size for PtAu/C than Pt/C (particle size 2–3 nm). In Fig. 4, the reduction feature around 0.4 V in the cathodic scan direction is attributed to the reduction of Pt oxide formed in the anodic scan direction (broad feature at > 0.6 V). However, the cathodic peak potential for reducing oxides on PtAu surface was found to shift negatively, linking to an electronic interaction between Pt and Au. In addition, the observation of the reduction peak at 0.95 V during the negative scan reflects the reduction of gold oxide species, which confirms the presence of Au in the PtAu/C electrocatalysts [16,34–36].

The electrocatalytic activities of Pt/C (*J–M*) and $Pt_{100-m}Au_m$/C catalysts for FA oxidation were investigated in deaerated 0.5 M H_2SO_4 + 1 M FA solution. A set of voltammogram curves is presented in Fig. 5A. Current densities in the voltammogram were normalized to the total mass of Pt and Au metals. For Pt/C (*J–M*) catalyst, the usual characteristics of Pt electrode in FA electrooxidation were observed, which can be ascribed to the dual-pathway mechanism [10]. The FA oxidation commenced at the potential more positive than the hydrogen desorption region in the positive scan direction showing a peak at about 0.3 V. The observation of this peak suggests that FA oxidation at low potentials occurs through the direct path with the simultaneous formation of CO_{ad} in the indirect path [37]. Increasing coverage of CO_{ad} reduces the amount of Pt surface available for the direct path. At the potential $E > 0.4$ V, the reaction significantly accelerates due to the oxidative removal of CO_{ad} by oxygen containing species on Pt, displaying a current maximum at 0.7 V. The ratio between the two peak currents sheds

Table 1
Summary of the size and composition data for the bimetallic catalysts.

Catalysts	ESA ($m^2\ g^{-1}$ Pt)	Particle diameter determined by TEM (nm)	Particle diameter determined by XRD (nm)	Atomic rations determined by ICP-AES
Pt/C	58.6	–	–	–
Pt–Au/C (70:30)	53.3	4.5	4.6	71.07:29.93
Pt–Au/C (60:40)	44.8	4.8	5.1	59.29:40.71
Pt–Au/C (50:50)	52.2	4.5	4.9	49.44:50.55
Pt–Au/C (40:60)	45.5	4.7	5.1	38.29:61.71
Pt–Au/C (30:70)	37.3	5.1	5.5	29.61:70.39

light on the question of which reaction pathway is dominant during the oxidation of FA.

In contrast, the polarization curves for PtAu bimetallic catalysts exhibited a different behavior in which the relative ratio of the two peak currents was dependent on the bimetallic composition. For $Pt_{60}Au_{40}$/C catalyst, the peak current at about 0.3 V is four times higher than that for Pt/C. At about 0.7 V, a small shoulder peak was observed in the anodic scan similarly to that for Pt/C, indicative of the formation of CO_{ad} poisoning intermediate. On the $Pt_{50}Au_{50}$/C and $Pt_{40}Au_{60}$/C catalysts, the peak potentials were also observed at about 0.3 V. Furthermore, $Pt_{50}Au_{50}$/C exhibits a very high mass activity ($8\ A\ mg^{-1}$), which is eight times higher than that of the Pt/C catalyst. Our catalyst showed an increase of specific activity by a factor of 9 and an increase of mass activity by a factor of 8 in comparison with those for Pt/C catalyst, which are higher than most reported in the literature. More importantly, the absence of a second anodic peak at a more positive potential indicates little CO generation/adsorption during FA electrooxidation. It is possible that the structure of gold atoms surrounding Pt atoms in the PtAu alloy with a relatively high percentage of Au has played an important role in the suppression of CO_{ad} formation.

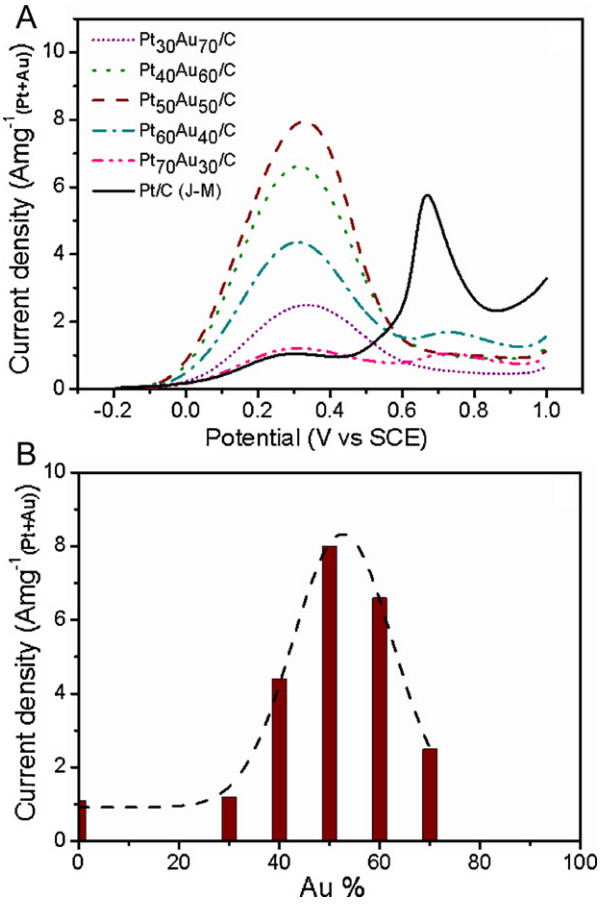

Fig. 5. (A) Cyclic voltammograms for $Pt_{100-m}Au_m$/C catalysts in N_2-saturated 0.5 M H_2SO_4 + 1 M FA solution with a scan rate of $50\ mV\ s^{-1}$. (B) Mass-specific current densities vs. bimetallic composition for PtAu/C.

The correlation between the composition and the electrocatalytic activity for the above catalysts is further assessed by analyzing the mass activity (i.e., the peak current density per unit total mass of metals). Fig. 5B summarizes a representative set of results showing the correlation between the mass activity and the bimetallic composition of PtAu/C for FA electrooxidation. The dash lines show the general trend in the composition range of PtAu alloy nanoparticles. The mass activity clearly exhibits a maximum around the composition of 50–60% Au. This finding suggests that this optimal fraction of Au and Pt atoms possibly led to an ordered surface arrangement of the metals responsible for the synergistic (electronic and ensemble) effect [38]. A similar synergistic effect was reported for the electrocatalytic methanol oxidation on gold–platinum nanoparticle catalysts [39], which, though not directly relevant to the enhanced direct path, demonstrate the important of electronic effect of the bimetallic surface on CO adsorption.

The above experimental results provided important information for understanding the origin of the enhanced electrocatalytic activity of PtAu surfaces toward FA oxidation. Enhancement of the FA oxidation on Pt by the addition of the second metal can be caused by the favorable dehydrogenation reaction, or by the efficient removal of CO_{ad} formed in the dehydration path. Several mechanisms have been proposed in the literature to explain their role. Here the electrocatalytic activity of the PtAu surfaces toward FA oxidation is discussed with respect to reported mechanisms. In acidic electrolytes, Au is not effective in producing surface oxygenated species to facilitate oxidation of $CO_{ad,}$ and therefore the bi-functional effect alone could not be responsible for the enhanced electrocatalytic activity of the PtAu alloy surfaces in the FA oxidation [40]. However there is a possibility that its presence on the surface weakens the bond between Pt and CO_{ad}. To test this possibility, CO was pre-adsorbed on pure Pt and PtAu surfaces and then oxidized in the CO-free electrolyte. Fig. 6A shows the voltammograms for Pt and PtAu alloy nanoparticles with adsorbed CO species on the surfaces. The shapes of all peaks were symmetrical, which is consistent with the single alloy property of PtAu surfaces as evidenced by the XRD data. Interestingly, the CO electrooxidation peak potentials shift toward higher potentials on PtAu/C compared to Pt/C, in agreement with previous observations on PtAu alloy and Pt-decorated Au nanoparticles [37,40,41]. As shown by the plots of the peak potential (E_p) and the integrated charge (Q_p) vs. the Au atomic fraction in the bimetallic catalysts (Fig. 6B), it is apparent that the positive shift of the peak potentials is accompanied by the gradual decrease of the amount of CO adsorbed on the catalyst surfaces. The decrease in the adsorbed CO species is basically leveled off at 50%Au, at which the positive shift of the peak potential also seems to show a subtle indication of leveling-off before further shift. While a detailed understanding of this correlation needs an in-depth study of the surface structure–reactivity relationship and the dynamics of oxidation of CO process, the CO stripping data led us to believe that the presence of Au does not facilitate oxidation of CO on PtAu surfaces.

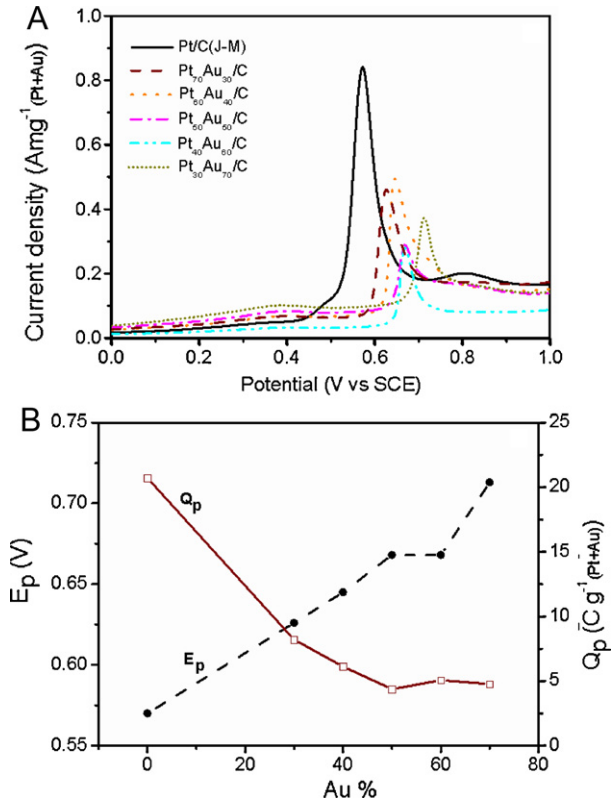

Fig. 6. (A) CO stripping voltammograms on Pt and PtAu electrodes in 0.5 M H_2SO_4 recorded for the first scan at a scan rate of 20 mV s^{-1}. (B) Plots of the peak potential (E_p) and the integrated charge (Q_p) vs. the Au atomic fraction in the bimetallic catalysts. The integrated charge in the voltammogram was normalized to the total mass of Pt and Au metals.

Recent density functional theory (DFT) calculations indicated the d-band shift for Pt in a PtAu surface because of higher electronegativity of Au than Pt [42,43], which was also in fact supported by high-resolution XPS data [44]. In addition, the alloy property of Pt and Au results in a tensile strain because of the larger lattice constant of Au than that of Pt. Both effects lead to the stronger adsorption of CO_{ad} on Pt. Moreover, Cuesta et al. have shown that the dehydration of FA to CO_{ad} requires at least three adjacent Pt atoms, whereas the dehydrogenation path requires at most two Pt atoms [45]. Also, the previous CV results demonstrated that the dehydration pathway was likely suppressed when the ratio of Pt to Au reached an appropriate value (Pt:Au $\leq$ 1). Therefore, our proposed mechanism for the enhanced electrocatalytic activity of PtAu/C catalysts is consistent with an ensemble effect in which the decreased availability of adjacent Pt atoms on PtAu surface leads to a complete suppression of the poisoning of the catalyst by the intermediate CO species.

To further evaluate the activity and stability of the PtAu/C catalysts for FA electrooxidation, we compared the current–time curves of selected PtAu/C catalysts with that of commercial Pt/C catalysts at 0.1 V (Fig. 7). The initial current density for $Pt_{50}Au_{50}$/C is 3.3 A mg^{-1}, which is more than three and six times larger than those of $Pt_{60}Au_{40}$/C and Pt/C catalysts, respectively. At the beginning of the current–time curves (<100 s), it can be seen that the current decays very rapidly for all the catalysts. After 2000s, the current density for $Pt_{50}Au_{50}$/C is 1.9 A mg^{-1}, which is about eight times larger than that for Pt/C. It is clear that the $Pt_{50}Au_{50}$ catalyst maintained a catalytic activity higher than the other catalysts in the chronoamprometric time frame. The observed gradual decrease of the oxidation current indicates that the $Pt_{50}Au_{50}$ catalyst might be unstable in the examined time frame. Considering the complications due to changes in reactant and product concentrations in the chronoamprometric measurement, a more appropriate assessment of the catalyst stability should be performed in fuel cells, which is part of our future work.

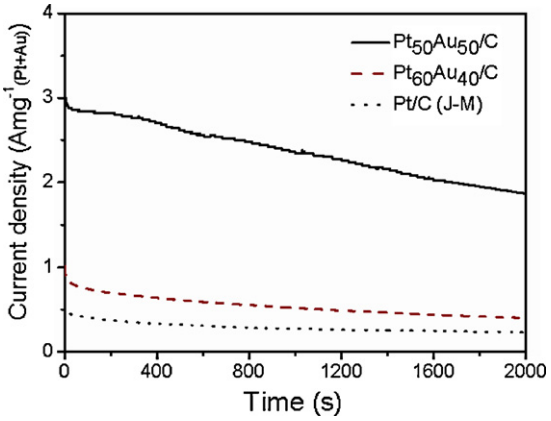

Fig. 7. Current–time curves recorded at 0.1 V (vs. SCE) for FA electrooxidation on $Pt_{60}Au_{40}$/C, $Pt_{50}Au_{50}$/C and commercial Pt/C catalysts in 0.5 M FA + 0.5 M H_2SO_4.

4. Conclusion

In summary, $Pt_{100-m}Au_m$/C catalysts with well-controlled size and bimetallic composition have been prepared, which has enabled us to establish the correlation between the bimetallic composition and the electrocatalytic activity for FA electrooxidation. The results of the systematic characterization of the $Pt_{100-m}Au_m$/C catalysts indicate that $Pt_{50}Au_{50}$/C is the optimum catalyst for the FA electrooxidation. An ensemble effect arising from the Au promoter in the bimetallic surface sites is responsible for the enhancement of the electrocatalytic activity for FA electrooxidation. In addition to the fundamental insight, our work has demonstrated an effective route for preparing nanoscale alloys of Pt with Au with well-controlled size and composition as a promising catalyst for FA electrooxidation and other catalytic reactions. This route also constitutes the basis for fabricating other bimetallic alloy catalysts for application in direct formic acid fuel cells.

Acknowledgements

The authors would like to thank the National Natural Science Foundation of China (Grant NSFC 20973140) for financial support. Part of the support for SUNY-Binghamton is from National Science Foundation (CBET-0709113). We also thank Prof. Z.B. Chen (Department of analytical chemistry, Xiamen University) for her help in conducting the ICP-AES measurements, and Dr. Q.L. Li (Department of Chemical Engineering, Xiamen University) for assistance in XRD analysis.

References

[1] X.W. Yu, P.G. Pickup, J. Power Sources 182 (2008) 124–132.
[2] Y.W. Rhee, S.Y. Ha, R.I. Masel, J. Power Sources 117 (2003) 35–38.
[3] Y.M. Zhu, Z. Khan, R.I. Masel, J. Power Sources 139 (2005) 15–20.
[4] H. Lee, S.E. Habas, G.A. Somorjai, P. Yang, J. Am. Chem. Soc. 130 (2008) 5406–5407.
[5] X.L. Ji, K.T. Lee, R. Holden, L. Zhang, J.J. Zhang, G.A. Botton, M. Couillard, L.F. Nazar, Nat. Chem. 2 (2010) 286–293.
[6] S. Uhm, H. Lee, Y. Kwon, J. Lee, Angew. Chem. Int. Ed. 47 (2008) 10163–10166.
[7] N. Hoshi, K. Kida, M. Nakamura, M. Nakada, K. Osada, J. Phys. Chem. B 110 (2006) 12480–12484.
[8] P.K. Babu, H.S. Kim, J.H. Chung, E. Oldfield, A. Wieckowski, J. Phys. Chem. B 108 (2004) 20228–20232.
[9] J.S. Gullón, V. Montiel, A. Aldaz, J. Clavilier, Electrochem. Commun. 4 (2002) 716–721.

[10] S.G. Sun, J. Clavilier, J. Electroanal. Chem. 240 (1988) 147–159.
[11] X. Li, I.M. Hsing, Electrochim. Acta 51 (2006) 3477–3483.
[12] E.C. Rivera, A.C.D. Angelo, C. Lind, F.J. Disalvo, Chem. Phys. Chem. 4 (2003) 193–199.
[13] F. Matsumoto, C. Roychowdhury, F.J. DiSalvo, H.D. Abruñ, J. Electrochem. Soc. 155 (2008) B148–B154.
[14] X.W. Yu, P.G. Pickup, Electrochim. Acta 55 (2010) 7354–7361.
[15] A.V. Tripković, K.Dj. Popović, K.Dj. Popović, J.D. Lović, A. Kowal, Electrochim. Acta 53 (2007) 887–893.
[16] W. Chen, J. Kim, S. Sun, S. Chen, Langmuir 23 (2007) 11303–11310.
[17] S. Zhang, Y.Y. Shao, G.P. Yin, Y.H. Lin, J. Power Sources 195 (2010) 1103–1106.
[18] A.V. Tripković, K.Dj. Popović, R.M. Stevanović, R. Socha, A. Kowal, Electrochem. Commun. 8 (2006) 1492–1498.
[19] J.B. Xu, T.S. Zhao, Z.X. Liang, J. Power Sources 185 (2008) 857–861.
[20] S.Y. Wang, N. Kristian, S.P. Jiang, X. Wang, Electrochem. Commun. 10 (2008) 961–964.
[21] Z.M. Peng, H. Yang, Nano Res. 2 (2009) 406–415.
[22] S. Zhang, Y.Y. Shao, G.P. Yin, Y.H. Lin, Angew. Chem. Int. Ed. 49 (2010) 2211–2214.
[23] R.Y. Wang, C. Wang, W.B. Cai, Y. Ding, Adv. Mater. 22 (2010) 1–4.
[24] J.S. Huang, H.Q. Hou, T.Y. You, Electrochem. Commun. 11 (2009) 1281–1284.
[25] J.H. Choi, K.J. Jeong, Y. Dong, J. Han, T.H. Lim, J.S. Lee, Y.E. Sung, J. Power Sources 163 (2006) 71–75.
[26] J.K. Lee, J. Lee, J. Hanc, T.H. Limc, Y.E. Sung, Y. Tak, Electrochim. Acta 53 (2008) 3474–3478.
[27] J. Luo, M.M. Maye, V. Petkov, N.N. Kariuki, L. Wang, P. Njoki, D. Mott, Y. Lin, C.J. Zhong, Chem. Mater. 17 (2005) 3086–3091.
[28] B.N. Wanjala, J. Luo, P.N. Njoki, M. Engelhard, H.R. Naslund, O. Malis, C.J. Zhong, Chem. Mater. 22 (2010) 4282–4294.
[29] J. Luo, M.M. Mayea, N.N. Kariuki, L.Y. Wanga, P. Njoki, Y. Lina, M. Schadt, H. Richard Naslundb, C.J. Zhong, Catal. Today 99 (2005) 291–297.
[30] J. Luo, P.N. Njoki, Y. Lin, L.Y. Wang, C.J. Zhong, Electrochem. Commun. 8 (2006) 581–587.
[31] M.J. Hostetler, C.J. Zhong, B.K.H. Yen, J. Anderegg, S.M. Gross, N.D. Evans, R.W. Murray, J. Am. Chem. Soc. 120 (1998) 9396–9397.
[32] M.M. Maye, N.N. Kariuki, J. Luo, L. Han, P. Njoki, L. Wang, Y. Lin, H.R. Naslunda, C.J. Zhong, Gold Bull. 37 (2004) 217–223.
[33] K.J.J. Mayrhofer, D. Strmcnik, B.B. Blizanac, V. Stamenkovic, M. Arenz, N.M. Markovic, Electrochim. Acta 53 (2008) 3181–3188.
[34] I.S. Park, K.S. Lee, D.S. Jung, H.Y. Park, Y.E. Sung, Electrochim. Acta 52 (2007) 5599–5605.
[35] Y.W. Ma, H.M. Zhang, H.X. Zhong, T. Xu, H. Jin, X.Y. Geng, Catal. Commun. 11 (2010) 434–437.
[36] Y.J. Hu, H. Zhang, P. Wu, H. Zhang, B. Zhou, C.X. Cai, Phys. Chem. Chem. Phys. 13 (2011) 4083–4094.
[37] F.J.E. Scheijen, G.L. Beltramo, S. Hoeppener, T.H.M. Housmans, M.T.M. Koper, J. Solid State Electrochem. 12 (2008) 483–495.
[38] I.S. Park, K.S. Lee, J.H. Choi, H.Y. Park, Y.E. Sung, J. Phys. Chem. C 111 (2007) 19126–19133.
[39] D. Mott, J. Luo, P.N. Njoki, Y. Lin, L. Wang, C.J. Zhong, Catal. Today 122 (2007) 378–385.
[40] M.D. Obradovića, A.V. Tripkovića, S.L. Gojkovićb, Electrochim. Acta 55 (2009) 204–209.
[41] A. Habrioux, W. Vogel, M. Guinel, L. Guetaz, K. Servat, B. Kokoh, N.A. Vante, Phys. Chem. Chem. Phys. 11 (2009) 3573–3579.
[42] J. Greeley, J.K. Norskov, M. Mavrikakis, Annu. Rev. Phys. Chem. 53 (2002) 319–348.
[43] B. Hammer, J.K. Norskov, Adv. Catal. 45 (2000) 71–129.
[44] C. Berg, H.J. Venvik, F. Strisland, A. Ramstad, A. Borg, Surf. Sci. 409 (1998) 1–15.
[45] A. Cuesta, M. Escudero, B. Lanova, H. Baltruschat, Langmuir 25 (2009) 6500–6507.